Heliyon 10 (2024) e40990

Contents lists available at ScienceDirect

Heliyon

journal homepage: www.cell.com/heliyon

Research article

Effect of ionic liquid as a surfactant in hydroxyapatite coatings for improvement corrosion resistance of Ti-6Al-4V substrates for implant applications

Meysam Safari-Gezaz, Mojtaba Parhizkar *

Department of Condensed Matter Physics, Faculty of Physics, University of Tabriz, 29 Bahman Blvd., Tabriz, Iran

ARTICLE INFO

Keywords:
Hydroxyapatite
Corrosion
Microemulsion
Ionic liquid
SBF

ABSTRACT

Research on hydroxyapatite (HAP) coatings for bone tissue applications has been investigated for decades due to their significant osteoconductive and bioactivity properties. HAP closely resembles the mineral component of human bone, making it ideal for biomedical applications such as implants. This study investigates the synthesis of hydroxyapatite nanoparticles (HAP-NPs) via the microemulsion method, which is essential for creating HAP coatings on the Ti-6Al-4V substrate. A variety of surfactants, including ionic liquid (IL; 2-hydroxyethyl ammonium octanoate ([HEA]OC)) and sodium lauryl sulfate (SLS), were employed to control the nucleation and crystal growth of HAP-NPs. The synthesized nanoparticles were dispersed in isopropanol and applied to the Ti-6Al-4V using the spin coating technique for creating HAP coatings. The samples were characterized using techniques such as FTIR, HNMR, XRD, FESEM, EDS, and AFM. Tafel and Electrochemical impedance spectroscopy (EIS) analyses were used to evaluate the corrosion resistance of the coatings in a simulated body fluid (SBF). The use of IL as a surfactant led to a significant reduction in nanoparticle size from 37.32 nm to 24.80 nm, which is critical for enhancing the coating's properties. Surface roughness decreased dramatically from 84.28 nm to 12.48 nm, indicating a smoother coating that can improve the adhesion strength of coatings. Electrochemical tests demonstrated improved corrosion resistance of coatings, with the charge transfer resistance (R_{ct}) for the HAP-0.4 IL coating reaching 7.84 MΩ × cm^2, compared to 0.11 MΩ × cm^2 for the bare Ti-6Al-4V. [HEA]OC as a surfactant improved the protective quality and uniformity of the HAP-IL coatings and reduced the surface roughness. These results indicate that modifying the surface of Ti-6Al-4V with HAP-IL coatings is a promising approach for enhancing its performance in biomedical applications.

1. Introduction

Hydroxyapatite (HAP) is a significant inorganic component and a calcium phosphate-based material. It is commonly used in biomedical materials to restore damaged teeth and bones due to its exceptional features like bioactivity, biocompatibility, bone integration, non-toxicity, and osteo-reconstruction conductivity [1–3]. Furthermore, HAP is extensively utilized in multiple applications, including bone tissue engineering, slowing down cancer cell growth, purifying water, medical implants, drug delivery, ion conductors, and gas sensors [4–6]. A unique feature of HAP lies in its adaptability to adjust its structure in response to the surrounding

* Corresponding author. Faculty of Physics, University of Tabriz, Tabriz, Iran.
E-mail address: parhizkar@tabrizu.ac.ir (M. Parhizkar).

https://doi.org/10.1016/j.heliyon.2024.e40990
Received 13 July 2024; Received in revised form 4 December 2024; Accepted 4 December 2024
Available online 5 December 2024

environment, enabling seamless integration with natural tissues and enhancing the healing process [7–9]. Among the widely used metal biomaterials in medicine, titanium alloys play a prominent role [10]. To improve the biocompatibility of titanium alloys, biocompatible coatings are increasingly applied to enhance their biological properties [11]. One effective method involves the application of a hydroxyapatite coating to improve the surface properties of titanium implants, utilizing techniques like electrophoretic deposition, the sol-gel method, and vapour deposition [12,13].

The synthesis of HAP-NPs can be conducted through various methods such as sol-gel [14,15], co-precipitation [16,17], mechanochemical [18], hydrothermal method [19,20], ultrasonic irradiation [21], microwave-assisted irradiation [22]. While these methods may present challenges like irregular particle size distribution and non-uniform morphology, the microemulsion (ME) approach has emerged as a favorable option for HAP-NP synthesis [23–25]. The main advantages of this method could be simplicity, morphology control, higher thermodynamic stability, narrow size distribution, cost-effectiveness, and anti-aggregation [26,27]. Also, this approach provides better crystallinity without requiring extremely high temperatures. The microemulsion system is a solution containing a surfactant, a nonpolar phase (typically oil), and a polar phase (typically water) that is optically transparent and thermodynamically stable [28–30]. This method allows for precise control over nanoparticle size and morphology through adjustments in fundamental factors like surfactant concentration and the water-to-oil ratio [31].

Ionic liquids as surfactants and green solvents are organic electrolytes with special features that include high solvation capacity, non-flammability, high thermal stability, low melting points, high viscosity, etc. [32,33]. These organic electrolytes have a variety of applications, including the synthesis of crystalline nanostructured materials, biology, catalysts, supercapacitors, and electrochemistry [34–36]. The synthesis of ionic liquids has seen significant growth, utilizing biocompatible combinations such as carboxylic acids, glucose, and amino acids [37]. Monoethanolamine is commonly employed as the cationic component in biocompatible ionic liquids due to its biodegradability, affordability, and water solubility. The use of this organic chemical composition has enabled the preparation of biocompatible ionic liquids to be more cost-effective and led to the development of combinations with low toxicity and high biocompatibility [38]. ILs display considerable benefits as surfactants in HAP structures, thereby augmenting their functionality and potential for application. Their specific properties facilitate enhanced solubilization and catalytic efficiency, rendering them advantageous in a range of chemical processes. The advancement of environmentally friendly methods utilizing ILs could reduce toxicity and enhance the sustainability of HAP coatings manufacturing [39]. 2-hydroxyethyl ammonium octanoate ([HEA]OC) is a widely used IL in catalysis, electrochemistry, biomedicine, etc. [HEA]OC has considerable benefits, especially due to its biodegradable and non-toxic characteristics. This compound is an IL known for its low toxicity and high biodegradability, making it suitable for various applications with minimal environmental impact [40]. The synthesis of tris(2-hydroxyethyl)ammonium salts has demonstrated low toxicity, validating their pharmacological applications [41].

In our experimental study, spherical-shaped HAP-NPs were synthesized using the microemulsion method. Anionic surfactants, namely 2-hydroxyethyl ammonium octanoate ([HEA]OC) and SLS were used, with different concentrations of [HEA]OC. Subsequently, the HAP-IL nanoparticles were dispersed, and coatings were prepared using the spin coating technique for biomedical applications. Notably, this ionic liquid has been used to prepare hydroxyapatite coatings for the first time, showing improved functional properties.

2. Materials and methods

2.1. Materials

Monoethanolamine, octanoic acid, $Ca(NO_3)_2.4H_2O$, P_2O_5, SLS, n-hexane, triethanolamine, ethanol, isopropanol, and ammonium hydroxide as a precipitating agent were purchased from Merck. These chemicals were used as purchased, without any further purification. During the experimental process, deionized water (DI) was used. SBF prepared in advance was utilized as the corrosion solution [42].

2.2. Synthesis of [HEA]OC

The ionic liquid ([HEA]OC) with the cation 2-hydroxyethylammonium and the octanoate anion was synthesized through a straightforward acid-base neutralization process. For the synthesis of [HEA]OC, monoethanolamine was placed in a triple-necked glass flask equipped with a reflux condenser. The flask was mounted in an ice bath. The octanoic acid was added dropwise to the flask while being stirred with a magnetic stirrer. The stirring process was maintained at room temperature for 24 h to ensure the completion of the reaction. Fig. 1 shows the FT-IR and ^1H NMR spectra for the synthesis of [HEA]OC.

2.3. Preparation of HAP-NPs

HAP-NPs were prepared using the microemulsion method with the following steps: [HEA]OC (at concentrations of 0.1, 0.2, and 0.4 M) was chosen as a surfactant, while SLS served as the co-surfactant, and n-hexane acted as the oil phase. These solutions were dissolved in 40 mL of DI water under vigorous stirring for 1 h at 37 ° C to form an oil phase. Solutions of 0.3 M P_2O_5 and 0.5 M $Ca(NO_3)_2.4H_2O$, with a molar ratio of 1.67, were mixed for 2 h before being slowly added dropwise into the oil phase mixture. The solution was stirred vigorously for 2 h until a translucent solution was obtained. Subsequently, the pH of the mixture was adjusted to 10 by adding a 1.5M ammonia solution. After continuous stirring for 6 h, the suspension was left to age at room temperature for 24 h. The suspension was then filtered and washed five times with deionized water and ethanol. The resulting precipitates were dried at 120 ° C

for 24 h in an oven. Then the powder was calcined at 600 ° C for 3 h and sintered at 1100 ° C for 3 h to achieve pure hydroxyapatite.

2.4. Suspension preparation

Suspensions of pure HAP and HAP-IL with different concentrations of IL were obtained utilizing isopropanol as the solvent and triethanolamine (TEA) as the dispersant agent, at a total particle concentration of 10 g/L. After incorporating the necessary quantities of TEA into isopropanol, the HAP nanoparticles were added and subjected to magnetic stirring for around 12 h. Subsequently, they were subjected to ultrasonic sonication for 30 min prior to the coating process.

2.5. Substrate preparation

The Ti-6Al-4V substrates were cut into pieces measuring 10 mm × 10 mm × 3 mm and then underwent polishing in varying sizes. Initially, the substrates underwent a thorough rinsing with deionized water, followed by a meticulous cleansing process involving ultrasound treatment in acetone and ethanol for 30 min. Subsequently, the substrates were carefully dried using air. Hydrofluoric acid (HF) was employed as an etching treatment for a duration of 15 min to eliminate the oxide and scum present on the substrate's surface. Finally, all the substrates underwent a meticulous rinse in deionized water and were subsequently dried in the oven.

2.6. Preparation of coatings on the Ti-6Al-4V

Considering all kinds of coating techniques, the spin-coating technique is the best for it produces homogeneous and uniform thin layers with great precision. Unlike dip coating, plasma, and spraying techniques, the centrifugal force in the spin coating technique is used to distribute the suspensions homogeneously on the surface of the substrate. This technique can achieve layer thickness from a few nanometers up to several microns with high reproducibility and uniformity [43]. The Ti-6Al-4V substrates were coated with prepared suspensions using the spin coating technique at room temperature, which applied centrifugal force to create a thin layer. The coatings were formed with centrifugal forces for 25 s at 2500 RPM and then sintered at 400 °C for 2 h. The heat treatment applied to the coated substrates has a significant influence on the characteristics of the coatings. Sintering HAP coatings at 375 °C–500 °C enhances adhesion between Ti-6Al-4V and the coating [44].

2.7. Characterization

Synthesized samples were analyzed using Fourier transform infrared (FT-IR) and nuclear magnetic resonance (HNMR) spectroscopies (Bruker TENSOR 27, Bruker Avance 400 MHz, Germany, respectively). FTIR is used to identify functional groups and confirm the chemical composition of HAP-NPs, while HNMR offers insights into IL's molecular structure and dynamics. Phase identification and crystal structure analysis were conducted using X-ray diffraction (XRD) with a Siemens D500-Germany spectrometer equipped with Cu-K_α radiation. XRD is essential for evaluating the crystalline structure, and phase purity of HAP-NPs, which impact on their bioactivity and mechanical properties [45]. The average crystallite size of the samples was determined using the Debye-Scherrer equation as follows [46,47]:

$$D = 0.9\lambda/(\beta \cos\theta) \tag{1}$$

where λ is the wavelength of X-ray, β is their full width at half maximum in radians, and θ is the Bragg angle in degrees. Also, the hexagonal lattice parameters and the unit cell volume (V) of the obtained HAP powder were calculated using the following equations [15]:

$$\frac{1}{d^2} = \frac{4}{3}\left(\frac{h^2 + hk + k^2}{a^2}\right) + \frac{l^2}{c^2} \tag{2}$$

$$V = \frac{\sqrt{3}a^2c}{2} \tag{3}$$

where a and c are the lattice constants and h, k, and l are the Miller indexes.

The field emission scanning electron microscope (FESEM; Can Scan-Tescan MIRA3 FEG, check) was utilized to examine the surface morphology of the coatings, while energy-dispersive X-ray spectroscopy (EDS) was employed for elemental analysis. FESEM can analyze high-resolution surface morphology to illustrate microstructure and uniformity of coatings [48], which are important factors contributing to biocompatibility. EDS is a complement of FESEM analysis since through this technique it is possible to perform an elemental analysis for the confirmation of the composition and the distribution of elements within HAP coatings [49]. To examine the surface roughness of the coated substrates, atomic force microscopy (AFM) was employed using the Nanosurf Mobile S instrument from Switzerland. AFM is used to assess the surface topography at the nanoscale, affecting cell proliferation and adhesion on coatings [50].

2.8. In vitro electrochemical tests

The Autolab PGSTAT30 Potentiostat-Galvanostat was utilized for obtaining electrochemical data, and their analysis. All electrochemical experiments were conducted using a standard three-electrode cell in SBF as the electrolyte solution at room temperature. The working, counter, and reference electrodes employed were the coated samples, platinum wire, and Ag/AgCl (3 M KCl), respectively. To investigate the corrosion behavior of the samples, the Tafel polarization method was utilized with a scan rate of 1 mV S^{-1}. Additionally, electrochemical impedance experiments were carried out at the open circuit potential (OCP) within frequency ranges of 100 kHz to 10 mHz, with an amplitude of ±5 mV.

3. Results and discussion

3.1. Synthesis of 2-hydroxyethyl ammonium octanoate

3.1.1. FTIR and ^1H NMR analysis

The FT-IR spectra of the synthesized IL 2-hydroxyethylammonium octanoate are given in Fig. 1a. According to the FT-IR (KBr, cm^{-1}) spectra of IL, the OH and NH peaks of the ethanolamine group appeared at 3200–3550 cm^{-1} [51,52]. The strong specific long-chain alkyl group's bond at 2925 cm^{-1} corresponds to the asymmetric and symmetric vibration of CH_2 [53]. The COO^- absorption peaks can be seen at 522, 658, 723, and 2141 cm^{-1}. The bonds at 867 and 923 cm^{-1} were assigned to the vibration of the C-C bond [54]. The carboxylic acid carbonyl (C=O) peak appeared at 1308 and 1554 cm^{-1} [51]. The peaks at 1074 cm^{-1} was assigned to the asymmetric stretching vibration of CH_3 bond. The bonds approximately at 1025, 1170, and 1403 cm^{-1} represented the COOH in-plane, out-plane, and symmetric bending vibrations, respectively. ^1H NMR spectra of the synthesized ionic liquid are shown in Fig. 1b. ^1H NMR of ionic liquid 2-hydroxyethylammonium octanoate (400 MHz, D_2O) are as follow (ppm): 4.7 (4H, -NH^{3+} and -OH), 3.51 (2H, -CH_2), 2.82 (2H, -CH_2), 1.87 (2H, -CH_2), 1.27 (2H, -CH_2), 1.00 (8H, -CH_2-CH_2-CH_2-CH_2), 0.60 (3H, -CH_3).

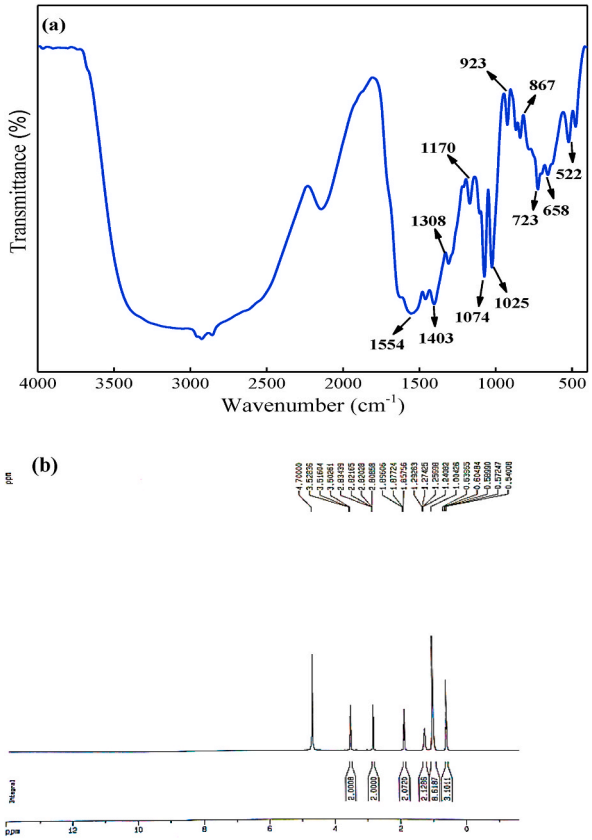

Fig. 1. FTIR and ^1H NMR spectra of the 2-hydroxyethyl ammonium octanoate.

3.2. Synthesis and characterization of hydroxyapatite nanoparticles

3.2.1. FTIR analysis

Fig. 2a–d shows typical FTIR spectra of the synthesized HAP samples with and without surfactant that were sintered at 1100 ° C. The sharp peaks observed at 630, 3561, and 3646 cm^{-1} were related to the stretching, symmetric, and asymmetric vibrations of lattice OH^- ions, respectively [55]. The bending vibration of the hydroxyl group appeared at 1648 cm^{-1} and the broad peak of adsorbed-lattice water was observed at 3415 cm^{-1} [56,57]. The characteristic bands of the PO_4^{3-} group appeared at 478, 566, 608, 961, 1036, and 1091 cm^{-1} [58]. The weak peak at 478 cm^{-1} was attributed to the bending mode (ν_2) of the PO_4^{3-} group, and the sharp peaks at 566 and 608 cm^{-1} could be assigned to the bending asymmetric vibration mode (ν_4) of the phosphate group [59]. The presence of the stretching vibration symmetry mode (ν_1) at 961 cm^{-1} is attributed to the phosphate group, and the strong bands that appeared at 1036 and 1091 cm^{-1} can be assigned to the asymmetric stretching vibration modes (ν_3) of the PO_4^{3-} groups [59]. Besides, the weak peak of O-H bending was found at 1432 cm^{-1}. The FT-IR results show that the prepared samples were synthesized with high purity and quality.

3.2.2. XRD analysis

X-ray diffraction (XRD) analysis was conducted to evaluate the purity and crystal structure of the synthesized specimens. Fig. 3 illustrates the XRD patterns of nanoparticles produced with varying concentrations of [HEA]OC, ranging from zero to 0.4 M. The main characteristic peaks at 2θ values of 25.79°, 31.71°, 32.17°, 32.90°, 34.03°, 39.80°, 46.66°, 49.47°, and 53.13° corresponding to the (002), (211), (112), (300), (202), (310), (222), (320), and (004) diffraction planes of hexagonal-structured HAP-NPs were observed in all four samples (Fig. 3a–d) [46,52]. These prominent peaks confirmed the synthesis of crystalline HAP, with no presence of additional crystalline phases. The XRD patterns closely matched the standard International Center for Diffraction Data (ICDD) file no. (09–0432) [60]. The [HEA]OC and SLS surfactants significantly impacted HAP-NP improvement, reducing the particle size from 37.32 nm to 24.80 nm, as calculated by the Debye-Scherrer equation. Briefly, increasing the [HEA]OC concentration significantly reduced the nanoparticle size of HAP.

Higher ionic liquid concentrations result in a reduction of the critical micelle concentration (CMC) of surfactants, which in turn produces smaller micelle sizes and improves the stabilization of nanoparticles [61]. Ionic liquids' unique characteristics enable a range of intermolecular interactions (e.g., van der Waals, and electrostatic forces), which enhance the self-organization of nanoparticles and promote their size reduction [62]. Table 1 presents the calculated lattice parameters (a, c), cell volumes, and average grain size of the HAP and surfactant-assisted HAP. The obtained lattice parameters and cell volumes of the synthesized HAP-NPs showed good agreement with the standard JCPDS values.

3.2.3. FESEM studies

Fig. 4a–d illustrates the surface morphology of HAP coatings with different IL concentrations as a surfactant. Additionally, elemental mapping and coating thickness for HAP-0.4 IL were obtained from the FESEM cross-sectional image in Fig. 4e and f. In the pure HAP coating, large agglomerates of varying sizes were non-uniformly dispersed on the substrate surface (Fig. 4a). Fig. 4b–d shows FESEM images for different concentrations of [HEA]OC. Coatings prepared with [HEA]OC had a more uniform morphology and smaller agglomerates compared to pure HAP. The FESEM images indicate that increasing the [HEA]OC concentration from 0.1 M to 0.2 M improved surface morphology and reduced nanoparticle aggregation (Fig. 4b and c). However, the coating prepared with 0.4 M [HEA]OC, as shown in Fig. 4d, exhibited spherical nanoparticles with minimal agglomeration and a smooth, hole-free surface. The agglomerates were significantly smaller at this concentration than those at other concentrations. The combination of [HEA]OC (surfactant), SLS (co-surfactant), and n-hexane (oil) in an aqueous solution effectively reduced agglomeration and produced smaller particles. The existence of [HEA]OC promotes the uniform dispersion of HAP-NPs across the Ti-6Al-4V surface, resulting in obtaining a smooth surface. The uniform distribution of HAP-NP is essential for attaining a consistent coating thickness, which has a direct impact

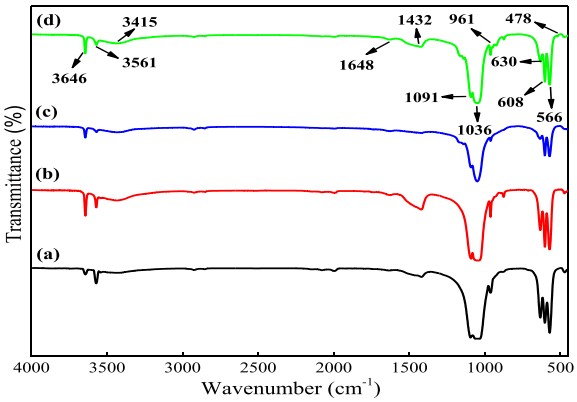

Fig. 2. FTIR spectra of the HAP powder prepared by microemulsion method: (a) pure HAP, (b) HAP-0.1 IL, (c) HAP-0.2 IL and (d) HAP-0.4 IL.

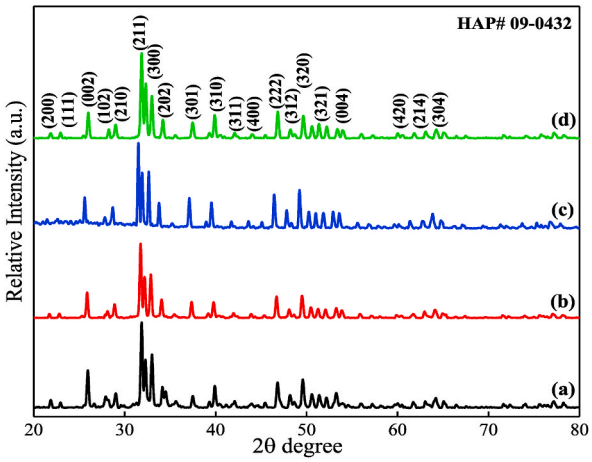

Fig. 3. XRD patterns of the HAP powder prepared by microemulsion method: (a) pure HAP, (b) HAP-0.1 IL, (c) HAP-0.2 IL and (d) HAP-0.4 IL.

Table 1
The crystal structure, Lattice parameters, unit cell volume and grain size of the HAP samples.

Sample code	Crystal structure	Lattice parameters (Å)		Unit cell	Average grain
		a = b		volume (Å^3)	size (nm)
Pure HAP	Hexagonal	9.42	6.86	527.17	37.32
HAP-0.1 IL	Hexagonal	9.44	6.87	530.18	32.43
HAP-0.2 IL	Hexagonal	9.44	6.85	528.64	30.71
HAP-0.4 IL	Hexagonal	9.43	6.88	529.83	24.80
Standard pure HAP	Hexagonal	9.41	6.88	528.80	

on the mechanical properties and biocompatibility of the implant [63]. Improved surface properties, including decreased porosity and agglomeration, significantly enhance the adhesion between the Ti-6Al-4V substrate and the HAP coatings [64]. FESEM images confirm that 0.4 M ionic liquid is optimal for achieving coatings with uniform morphology. Surfactants gain the increase in dispersion of nanoparticles within the coating matrix by changing their surface properties [65]. Stabilizing nanoparticles with surfactant prevents agglomeration and allows more appropriate coating applications [66]. Elemental mapping was performed to evaluate the distribution of Ca, P, and O on the coating surface of HAP-0.4 IL as the optimal sample (Fig. 4e). The qualitative assessment showed a uniform distribution of these elements across the surface. Fig. 4f illustrates the optimal coating thickness of HAP-0.4 IL in the FESEM cross-sectional image.

The coating thickness was approximately 1.31 μm. Coating thickness has major effects on enhancing the growth of bone tissues at the implant-bone interface area. A study found that a thinner HAP layer from plasma spray resulted in superior bone and fibrous tissue quality compared to a thicker layer (50 μm) [67]. Thin coatings may lack adequate mechanical support, whereas overly thick coatings can result in poor adhesion and increased stress at the interface [68,69]. Additionally, Fig. 5 presents the EDS analysis of the coatings, confirming the presence of calcium (Ca), oxygen (O), phosphorus (P), titanium (Ti), vanadium (V), and aluminum (Al) in all coatings.

3.2.4. Surface roughness

AFM analysis is an effective method for evaluating coatings in biomedical applications. AFM provides in-depth insights into the surface roughness, topography, and morphology of coatings, which is essential for determining biocompatibility and the potential for bacterial adhesion [70]. AFM images for all samples are shown in Fig. 6, with surface roughness measurements summarized in Table 2. Mean square roughness (R_q), average roughness (R_a), and total roughness (R_t) are measurements that represent the surface roughness of samples, all offering valuable insights into the coatings' surface characteristics.

The surface roughness of samples decreased from 84.28 nm to 12.48 nm, which can be attributed to the reduction of the size of nanoparticles and aggregates in the presence of surfactant. Table 2 results show that using ionic liquid reduced the surface roughness of the coatings. Consequently, it can improve the adhesion strength of the film/substrate, enhance the proliferation of osteoblast cells, and promote bone growth [71]. The surface roughness of HAP coatings can affect the adhesion and proliferation of osteoblast cells. A smoother surface is more favorable for cell attachment, proliferation, and in vitro cell spreading. The reason is that cells spread more easily on smoother surfaces. Therefore, the higher the cell-substrate interaction, the higher the proliferation rate of osteoblast cells that might occur on smoother HAP coatings. Osteoblasts are responsible for bone formation. Consequently, an increase in their proliferation results in increased bone growth [72,73]. Research indicates that smooth, and uniform surfaces have better corrosion resistance. Valadez-Martínez et al. demonstrated that reducing the roughness of coatings enhances their corrosion resistance [74].

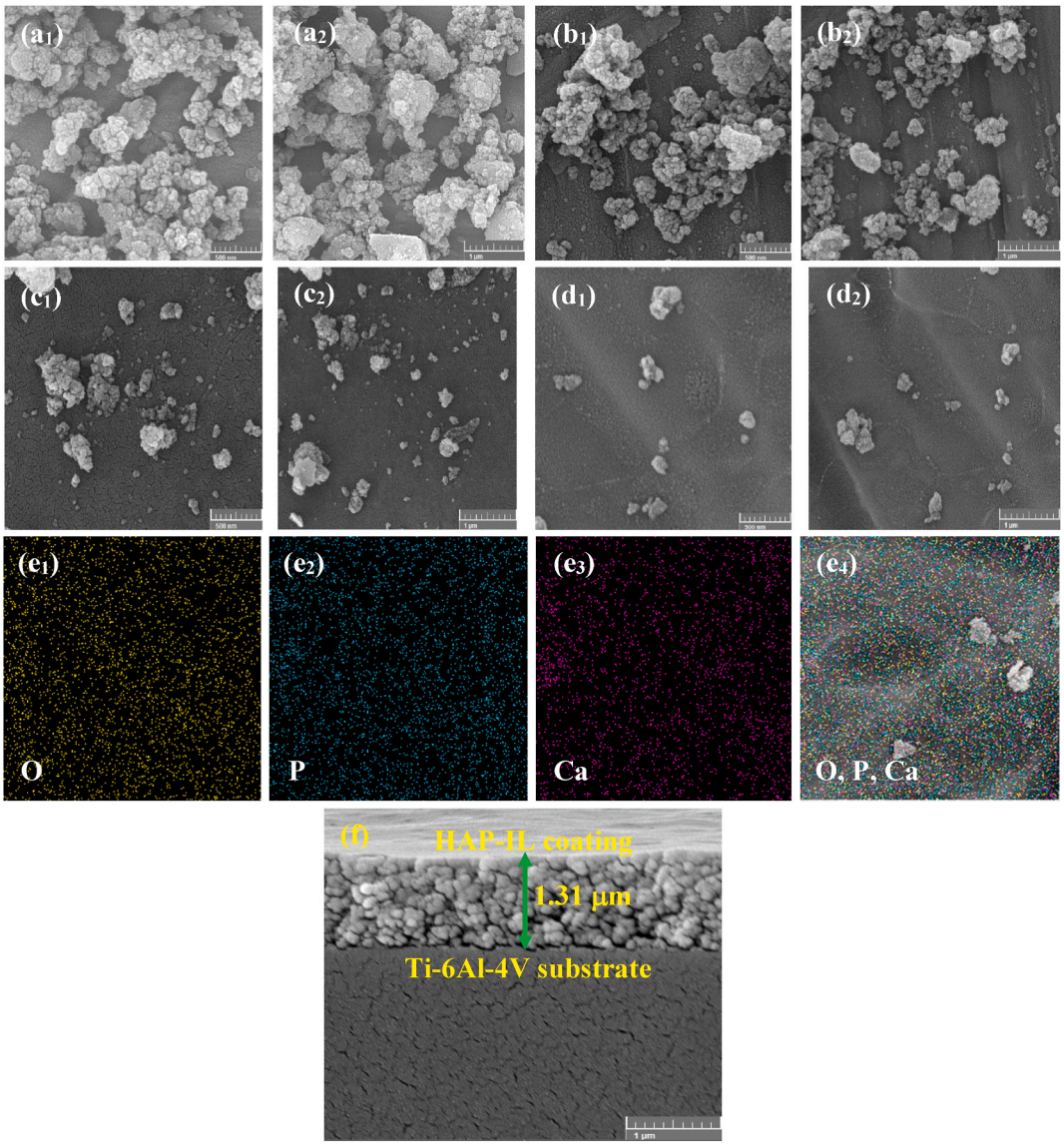

Fig. 4. FESEM images of HAP coatings at various [HEA]OC concentrations: (a) pure HAP, (b) 0.1 M, (c) 0.2 M, and (d) 0.4 M [HEA]OC, (e) elemental mapping for the HAP-0.4 IL sample, and (f) coating thickness for the HAP-0.4 IL sample.

3.2.5. In vitro corrosion studies

3.2.5.1. Tafel polarization. One of the main problems with the use of biomedical implants inside the human body is their corrosion rate. Therefore, the samples' corrosion resistance was assessed using Tafel polarization studies after 5 h of immersion in a solution of SBF. The results of these experiments are displayed in Fig. 7A, which includes parameters such as corrosion current density (i_{corr}), polarization resistance (R_p) and corrosion potential (E_{corr}), and the corresponding data are presented in Table 3. Also, Fig. 7B shows the variations in R_p and i_{corr} from Tafel analyses. Tafel tests were carried out under the same conditions for all samples. As can be seen in Fig. 7A, there are significant differences between coated specimens and substrate in the Tafel measurement. The coated samples from the substrate exhibit anodic current differences of greater than 1-2 orders of magnitude. As seen in Fig. 7A, the coatings produced with nanoparticles that were synthesized by ionic liquid exhibit a notable shift towards low i_{corr}.

This shift can be attributed to the uniform surface of the coatings in the presence of surfactants. According to the FESEM images (Fig. 4), the presence of surfactants reduced the agglomerates and increased the uniformity of the coatings' surface. Furthermore, synthesized nanoparticles with ionic liquid caused a decrease in nanoparticle size. The uniform distribution of nanoparticles and decreases in the nanoparticle size cause the creation of a crack-free and uniform coating that prevents penetration of aggressive solution to the Ti-6Al-4V. Ions diffusion from the SBF electrolyte caused an increase of i_{corr} for the Ti-6Al-4V compared to the coated samples. As a result, the increase in corrosion protection of the samples is shown by the decrease in their i_{corr} [75]. The polarization

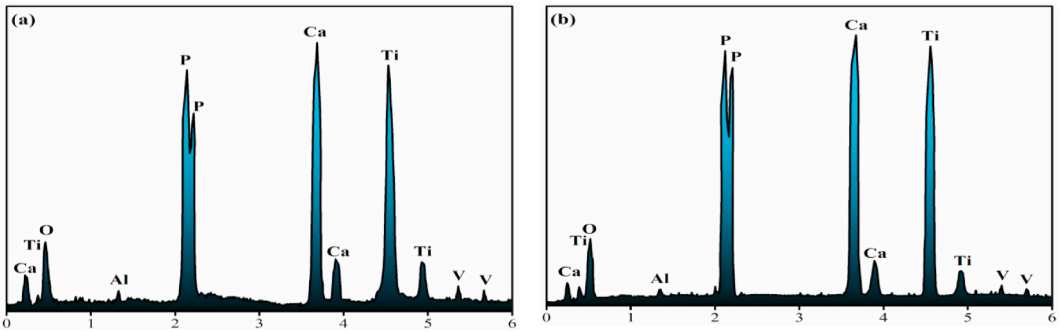

Elt	Ca	P	O	Ti	Al	V
wt. %	18.37	11.21	36.21	28.69	3.11	2.41

Elt	Ca	P	O	Ti	Al	V
wt. %	19.72	11.81	33.72	29.73	2.75	2.27

Elt	Ca	P	O	Ti	Al	V
wt. %	17.36	10.49	39.41	27.15	3.34	2.25

Elt	Ca	P	O	Ti	Al	V
wt. %	18.78	11.65	37.81	28.64	1.91	1.21

Fig. 5. EDS analysis (a) Pure HAP, (b) HAP-0.1 IL, (c) HAP-0.2 IL, and (d) HAP-0.4 IL of the coatings.

resistance increased from 0.097 MΩ × cm^2 for the Ti-6Al-4V to 3.334 MΩ × cm^2 for the HAP-0.4IL coating. Additionally, pure HAP coating has lower polarization resistance than other coated samples, likely due to agglomerates and the unevenness of the coating surface.

The efficiency of the corrosion barrier was evaluated using Eq. (5):

$$\eta\% = \frac{R_c - R_b}{R_c} \tag{5}$$

where R_b and R_c represent the R_p of the Ti-6Al-4V and coated coatings, respectively. We conducted Tafel tests within the potential range of −0.25V to +0.25V vs. OCP at a rate of 0.001 V/s. By Eq. (6), R_p was obtained from the Stern-Geary equation while i_{corr} was evaluated from the Butler-Volmer equation [76].

$$\boldsymbol{R_p} = \frac{\boldsymbol{\beta_c \beta_a}}{\boldsymbol{2.303\, I_{corr}(\beta_c + \beta_a)}} \tag{6}$$

According to Table 3, the HAP-0.4 IL coating exhibited the highest potential efficiency at 97.09 % compared to the other coatings, which can be selected as the optimal sample.

3.2.5.2. EIS studies. The EIS is a valuable technique for investigating the corrosion behavior and electrochemical performance of a coating in electrolytic solutions [77,78]. EIS experiments were carried out following a 5 h immersion of the coatings in the SBF solution (Fig. 8). Data from EIS were analyzed using equivalent circuits (ECs) illustrated in Fig. 8d and e, with distinct ECs employed for the Ti-6Al-4V and coated samples. These circuits feature R_s as the electrolyte resistance, while R_{coat} and R_{ct} represent the coating resistance and charge transfer resistance, respectively. The initial constant phase element denotes the coating's capacitance (CPE_{coat}), and the electrical double-layer capacitance (CPE_{dl}) is associated with the other time constant. The CPE, characterized by parameters Y_0 and n, represents the non-ideal behavior of solid electrodes as a substitute for conventional capacitors.

Fig. 8a shows the Nyquist plots for Ti-6Al-4V and coated samples. An increase in the diameter of the capacitor loop in the Nyquist

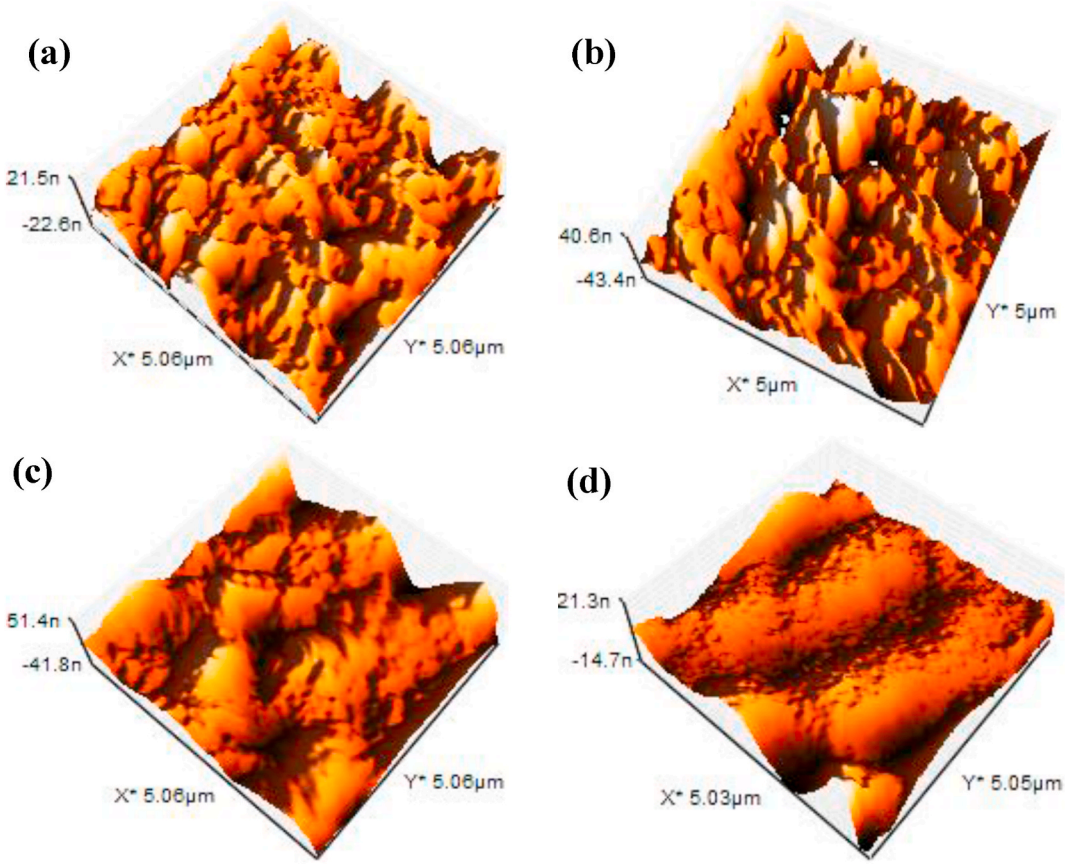

Fig. 6. 3-D topographical images from the coatings' surface using varying ionic liquid concentrations: (a) pure HAP, (b) HAP-0.1 IL, (c) HAP-0.2 IL, and (d) HAP-0.4 IL.

Table 2
Surface roughness of pure HAP and HAP with different concentrations of ionic liquid.

parameter	Pure HAP	HAP-0.1 IL	HAP-0.2 IL	HAP-0.4 IL
R_a [nm]	14.44	9.62	8.79	2.68
R_q [nm]	17.60	12.31	10.19	2.98
R_t [nm]	84.28	49.57	35.14	12.48

diagrams indicates an enhancement in the corrosion resistance of the coatings [79,80]. In comparison to Ti-6Al-4V, the coated samples significantly increased the diameter of the Nyquist plots in Fig. 8a. Also, the HAP-0.4 IL coating exhibits a bigger Nyquist plot diameter than the other coated samples, likely due to the reduced size of nanoparticles and surface agglomerates, which enhance barrier protection against aggressive solution penetration.

Charge transfer resistance (R_{ct}) is an important parameter in analyzing the anti-corrosion performance obtained from EIS measurements [81,82]. The Nyquist diagrams unveiled the highest R_{ct} value of 7.84 MΩ × cm^2 for the HAP-0.4 IL coating, while the charge transfer resistance of the substrate obtained 0.11 MΩ × cm^2. The increase in R_{ct} is largely influenced by the formation of passive layers on metallic surfaces that may modify the electrochemical behavior of the surface [83,84]. Passive layers, such as thin films act as barriers that affect charge transfer. Studies concerning thin layer-modified electrodes have indicated that the presence of non-electroactive layers can reduce the diffusion coefficient and solubility of electroactive species and thus result in increased R_{ct} [85]. Additionally, the corrosion resistance of coatings can be attributed to their microstructure, including nanoparticle distribution, surface uniformity, cracks, and porosity [86,87]. FESEM images are instrumental in assessing the uniformity and defect density of coatings, which are critical factors influencing their corrosion performance. Coatings that exhibit nonuniformity surface and higher defect densities typically show reduced resistance to corrosion [88]. Furthermore, research shows that modifications in coating composition and structure greatly enhance their protective properties [89]. Therefore, the FESEM results validate the electrochemical measurements, in which HAP-0.4 IL coating shows excellent corrosion resistance due to its uniform surface and larger capacitance loop diameter (Figs. 4 and 8).

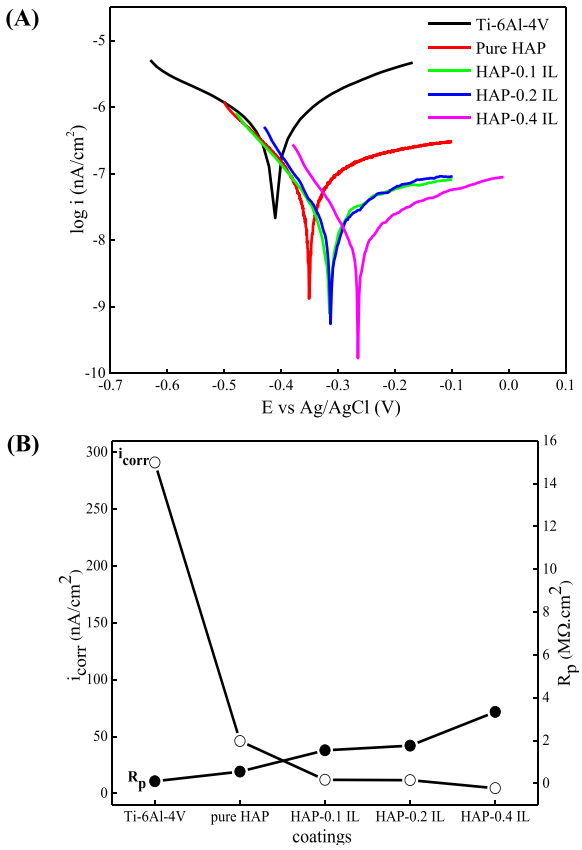

Fig. 7. (A) Polarization curves of Tafel and; **(B)** the changes in corrosion current density (i_{corr}) and polarization resistance (R_p) of coatings.

Table 3
Corrosion parameters of Ti-6Al-4V, pure HAP, and coatings of HAP-IL after 5 h immersion in SBF solution.

Sample	E_{corr} (mV vs. Ag/AgCl)	i_{corr} (nA/cm^2)	Ba (mV/dec)	Bc (mV/dec)	R_p (MΩ × cm^2)	η (%)
Ti-6Al-4V	−411.89	290.89	139.73	122.88	0.097	–
Pure HAP	−351.31	45.98	101.99	136.02	0.550	82.36
HAP-0.1 IL	−319.95	11.90	74.66	97.41	1.542	93.70
HAP-0.2 IL	−311.31	11.59	105.86	84.48	1.759	94.48
HAP-0.4 IL	−266.15	4.56	68.34	71.82	3.334	97.09

Examination of the Phase Bode diagrams in Fig. 8b and c revealed two different time constants, with the first corresponding to the coating and the latter to Ti-6Al-4V at lower frequencies. Larger magnitudes were seen in the Bode plots for the coated samples, particularly for the HAP-0.4 IL coating, suggesting the increase in corrosion protection of the coatings. Table 4 presents a summary of the electrochemical impedance data, which corresponds to previous literature findings [10,71]. For biomedical applications, implants with lower corrosion rates are appropriate within the body. The EIS analyses confirm that the HAP-0.4 IL coating demonstrates superior corrosion resistance compared to other samples, making it the best choice for biomedical applications. Table 5 compares the R_{ct}, I_{corr}, coating technique, and nanoparticle size results from this study with those in the existing literature, indicating that this study's outcomes are superior to previous findings.

4. Conclusion

Hydroxyapatite nanoparticles were successfully synthesized in this experimental work using the microemulsion method with different concentrations of [HEA]OC and a constant amount of SLS. These nanoparticles were then used to create coatings on Ti-6Al-4V substrates. FT-IR analysis showed pure peaks of HAP in the synthesized samples, indicating the absence of impurities. XRD results confirmed the successful synthesis of HAP-[HEA]OC nanoparticles with reduced particle sizes and without impurity phases. FESEM images demonstrated that using ionic liquid as a surfactant reduced surface agglomerates and nanoparticle size, yielding a more uniform coating surface. Elemental mapping confirmed the uniform distribution of oxygen, phosphorus, and calcium across the

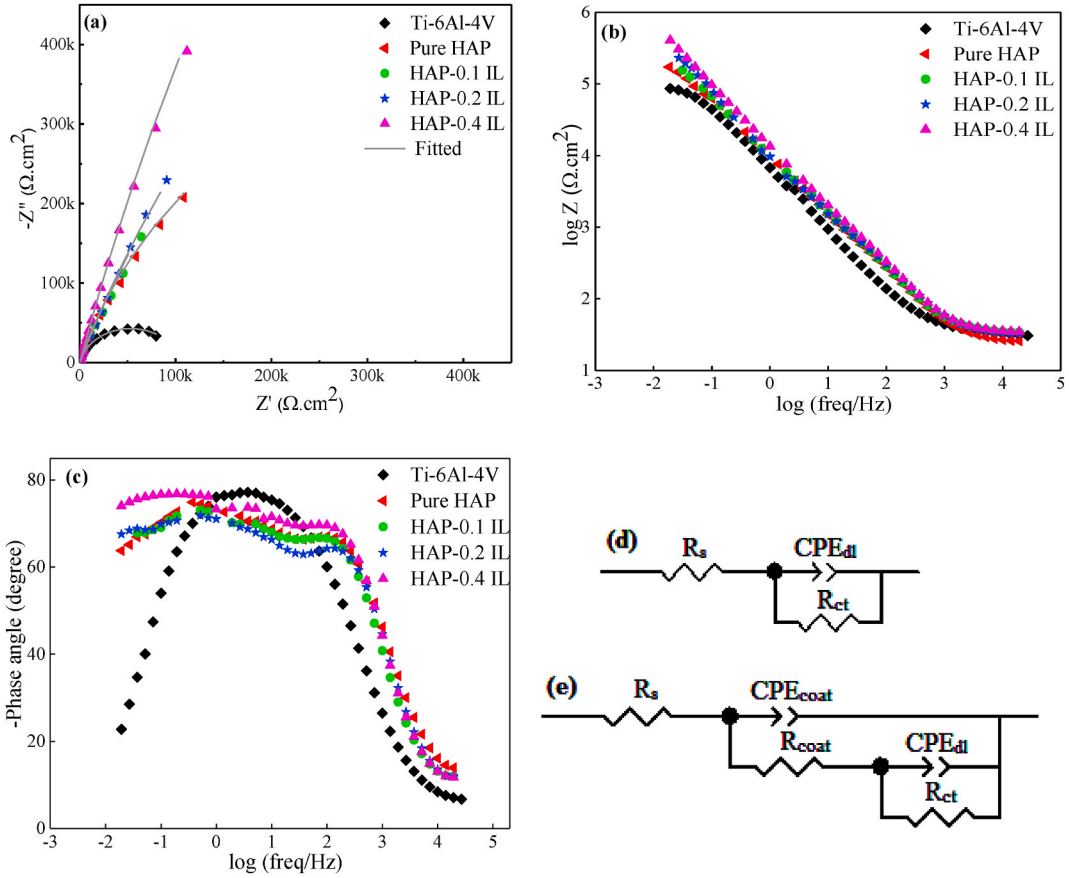

Fig. 8. (a) Nyquist plots; (b) Bode plots; (c) Phase plots for samples; the equivalent circuit used to analyze the EIS results for (d) Ti-6Al-4V, and (e) coatings.

Table 4
Electrochemical impedance values of Ti-6Al-4V, pure HAP, and coatings of HAP-IL with different ionic liquid concentrations at room temperature.

Sample	CPE_{coat}		R_{coat} ($k\Omega \times cm^2$)	CPE_{dl}		R_{ct} ($M\Omega \times cm^2$)	Fitting error
	$Y_0 \times 10^{-5}$ ($\Omega^{-1}cm^{-2}S^n$)	n		$Y_0 \times 10^{-5}$ ($\Omega^{-1}cm^{-2}S^n$)	n		
Ti-6Al-4V	–	–	–	2.93	0.86	0.11	0.00952
Pure HAP	1.86	0.82	5.38	0.36	0.87	1.12	0.00234
HAP-0.1 IL	1.7	0.83	5.48	0.42	0.70	3.13	0.00606
HAP-0.2 IL	1.17	0.86	1.35	1.1	0.75	3.45	0.00400
HAP-0.4 IL	1.14	0.87	5.21	0.39	0.84	7.84	0.00192

coatings. The coating thickness of the optimal sample (HAP-0.4 IL) was approximately 1.31 μm. AFM imaging demonstrated a significant decrease in surface roughness from 49.57 nm to 12.48 nm, attributed to the reduction in nanoparticle sizes and surface agglomerates. Electrochemical experiments showed that the decreased nanoparticle sizes and enhanced coating uniformity significantly reduced current density and enhanced corrosion resistance in the coatings. The utilization of a cost-effective and eco-friendly material to produce hydroxyapatite nanoparticles was successful. The HAP-IL coatings, especially HAP-0.4 IL, show enhanced surface uniformity and corrosion resistance, significantly increasing charge transfer resistance compared to bare Ti-6Al-4V after immersion in SBF. The current study gives important information on the characterization and optimization of HAP-IL coatings and underlines their potential biomedical applications.

CRediT authorship contribution statement

Meysam Safari-Gezaz: Writing – review & editing, Writing – original draft, Visualization, Validation, Software, Resources, Methodology, Investigation, Formal analysis, Data curation, Conceptualization. **Mojtaba Parhizkar:** Writing – review & editing, Writing – original draft, Visualization, Validation, Supervision, Software, Resources, Project administration, Methodology,

Table 5
Comparison of production coatings performance between this work and recent results.

nanoparticles	synthesis method	coating technique	nanoparticle size (nm)	i_{corr} (per cm^2)	R_{ct} (kΩ × cm^2)	Ref.
HA + PVA (0.05 %)	deposition	immersion	No data	0.46 μA	1.87	[90]
HA-Cip	sol-gel	spin-coating	72	10.2 nm	639	[91]
Ce/Si-HA	sol-gel	spin-coating (2000 rpm)	No data	253 μA	38.25	[71]
HA/PCL	purchased	dip coating	40	No data	200	[92]
HA (ATB2)	immersion	immersion	21	No data	1.24	[50]
Ti-75%WHA-25 % FBG	sol-gel and coprecipitation	electrophoretic deposition	200	97 nA	No data	[10]
HA	tooth-ash	magnetron sputtering	200	115 nA	289	[93]
HAP/TiO_2	PEO	PEO	No data	290 μA	11	[94]
hydroxyapatite	PEO	PEO	No data	2.8 μA	17	[95]
HA-35 kW	Clarion Pharmaceutical Co., India	plasma spray	500	90 nA	38	[96]
Ti-6Al-4V	**substrate**	**uncoated**	No data	**290.89 nA**	**110**	**This work**
Pure HAP	**microemulsion**	**spin-coating**	**37.32**	**45.98 nA**	**1120**	**This work**
HAP-0.4 IL	**microemulsion**	**spin-coating**	**24.80**	**4.56 nA**	**7840**	**This work**

Investigation, Formal analysis, Data curation, Conceptualization.

Data availability

All data generated or analyzed during this study are included in this published article.

Declaration of competing interest

The authors declare that they have no known competing financial interests or personal relationships that could have appeared to influence the work reported in this paper.

Acknowledgments

The financial support for this work from the University of Tabriz, Iran is gratefully acknowledged.

References

[1] Y. Sun, G. Guo, D. Tao, Z. Wang, Reverse microemulsion-directed synthesis of hydroxyapatite nanoparticles under hydrothermal conditions, J. Phys. Chem. Solid. 68 (2007) 373–377.
[2] J.-S. Li, Y. Li, X. Liu, J. Zhang, Y. Zhang, Strategy to introduce an hydroxyapatite–keratin nanocomposite into a fibrous membrane for bone tissue engineering, J. Mater. Chem. B 1 (2013) 432–437.
[3] J. Li, X. Liu, J. Zhang, Y. Zhang, Y. Han, J. Hu, Y. Li, Synthesis and characterization of wool keratin/hydroxyapatite nanocomposite, J. Biomed. Mater. Res. Part B Appl. Biomater. 100 (2012) 896–902.
[4] J. Gómez-Morales, J. Torrent-Burgues, T. Boix, J. Fraile, R. Rodríguez-Clemente, Precipitation of stoichiometric hydroxyapatite by a continuous method, Cryst. Res. Technol. J. Exp. Ind. Crystallogr. 36 (2001) 15–26.
[5] M. Eriksson, M. Andersson, E. Adolfsson, E. Carlström, Titanium–hydroxyapatite composite biomaterial for dental implants, Powder Metall. 49 (2006) 70–77.
[6] E. Andronescu, A. Ficai, M.G. Albu, V. Mitran, M. Sonmez, D. Ficai, R. Ion, A. Cimpean, Collagen-hydroxyapatite/cisplatin drug delivery systems for locoregional treatment of bone cancer, Technol. Cancer Res. Treat. 12 (2013) 275–284.
[7] N. Ribeiro, S.R. Sousa, F.J. Monteiro, Influence of crystallite size of nanophased hydroxyapatite on fibronectin and osteonectin adsorption and on MC3T3-E1 osteoblast adhesion and morphology, J. Colloid Interface Sci. 351 (2010) 398–406.
[8] F. Shi, Y. Liu, W. Zhi, D. Xiao, H. Li, K. Duan, S. Qu, J. Weng, The synergistic effect of micro/nano-structured and Cu2+-doped hydroxyapatite particles to promote osteoblast viability and antibacterial activity, Biomed. Mater. 12 (2017) 35006.
[9] B. El Ibrahimi, L. Guo, J.V. Nardeli, R. Oukhrib, The application of chitosan-based compounds against metallic corrosion, chitin chitosan-physicochem, Prop. Ind. Appl. 11 (2021) 231.
[10] S. Khanmohammadi, M. Ojaghi-Ilkhchi, M. Farrokhi-Rad, Development of bioglass coating reinforced with hydroxyapatite whiskers on TiO2 nanotubes via electrophoretic deposition, Ceram. Int. 47 (2021) 1333–1343.
[11] A. Bartkowiak, K. Suchanek, E. Menaszek, B. Szaraniec, J. Lekki, M. Perzanowski, M. Marszałek, Biological effect of hydrothermally synthesized silica nanoparticles within crystalline hydroxyapatite coatings for titanium implants, Mater. Sci. Eng. C 92 (2018) 88–95.
[12] N. Eliaz, N. Metoki, Calcium phosphate bioceramics: a review of their history, structure, properties, coating technologies and biomedical applications, Materials 10 (2017) 334.
[13] S. Komasa, Y. Taguchi, H. Nishida, M. Tanaka, T. Kawazoe, Bioactivity of nanostructure on titanium surface modified by chemical processing at room temperature, J. Prosthodont. Res. 56 (2012) 170–177.
[14] A. Bigi, E. Boanini, K. Rubini, Hydroxyapatite gels and nanocrystals prepared through a sol–gel process, J. Solid State Chem. 177 (2004) 3092–3098.
[15] M.S. Gezaz, S.M. Aref, M. Khatamian, Investigation of structural properties of hydroxyapatite/zinc oxide nanocomposites; an alternative candidate for replacement in recovery of bones in load-tolerating areas, Mater. Chem. Phys. 226 (2019) 169–176.
[16] S. Kannan, A.F. Lemos, J.M.F. Ferreira, Synthesis and mechanical performance of biological-like hydroxyapatites, Chem. Mater. 18 (2006) 2181–2186.

[17] A. Anwar, Q. Kanwal, S. Akbar, A. Munawar, A. Durrani, M. Hassan Farooq, Synthesis and characterization of pure and nanosized hydroxyapatite bioceramics, Nanotechnol. Rev. 6 (2017) 149–157.
[18] A. Fahami, B. Nasiri-Tabrizi, R. Ebrahimi-Kahrizsangi, Synthesis of calcium phosphate-based composite nanopowders by mechanochemical process and subsequent thermal treatment, Ceram. Int. 38 (2012) 6729–6738.
[19] S.-D. Jiang, Q.-Z. Yao, G.-T. Zhou, S.-Q. Fu, Fabrication of hydroxyapatite hierarchical hollow microspheres and potential application in water treatment, J. Phys. Chem. C 116 (2012) 4484–4492.
[20] A.A. Chaudhry, S. Haque, S. Kellici, P. Boldrin, I. Rehman, F.A. Khalid, J.A. Darr, Instant nano-hydroxyapatite: a continuous and rapid hydrothermal synthesis, Chem. Commun. (2006) 2286–2288.
[21] S. Manafi, S.H. Badiei, Effect of Ultrasonic on Crystallinity of Nano-Hydroxyapatite via Wet Chemical Method, 2008.
[22] P. Parhi, A. Ramanan, A.R. Ray, Synthesis of nano-sized alkaline-earth hydroxyapatites through microwave assisted metathesis route, Mater. Lett. 60 (2006) 218–221.
[23] Y. Wang, S. Zhang, K. Wei, N. Zhao, J. Chen, X. Wang, Hydrothermal synthesis of hydroxyapatite nanopowders using cationic surfactant as a template, Mater. Lett. 60 (2006) 1484–1487.
[24] G.C. Koumoulidis, A.P. Katsoulidis, A.K. Ladavos, P.J. Pomonis, C.C. Trapalis, A.T. Sdoukos, T.C. Vaimakis, Preparation of hydroxyapatite via microemulsion route, J. Colloid Interface Sci. 259 (2003) 254–260.
[25] C. Lai, S. Tang, Y. Wang, K. Wei, Formation of calcium phosphate nanoparticles in reverse microemulsions, Mater. Lett. 59 (2005) 210–214.
[26] M.-P. Pileni, The role of soft colloidal templates in controlling the size and shape of inorganic nanocrystals, Nat. Mater. 2 (2003) 145–150.
[27] K. El Mouaden, B. El Ibrahimi, R. Oukhrib, L. Bazzi, B. Hammouti, O. Jbara, A. Tara, D.S. Chauhan, M.A. Quraishi, Chitosan polymer as a green corrosion inhibitor for copper in sulfide-containing synthetic seawater, Int. J. Biol. Macromol. 119 (2018) 1311–1323.
[28] S. Shojaei, S.A. Hassanzadeh-Tabrizi, M. Ghashang, Reverse microemulsion synthesis and characterization of CaSnO3 nanoparticles, Ceram. Int. 40 (2014) 9609–9613.
[29] A. Zielińska, E. Kowalska, J.W. Sobczak, I. Łącka, M. Gazda, B. Ohtani, J. Hupka, A. Zaleska, Silver-doped TiO2 prepared by microemulsion method: surface properties, bio-and photoactivity, Sep. Purif. Technol. 72 (2010) 309–318.
[30] R. Pournajaf, S.A. Hassanzadeh-Tabrizi, M. Jafari, Reverse microemulsion synthesis of CeO2 nanopowder using polyoxyethylene (23) lauryl ether as a surfactant, Ceram. Int. 40 (2014) 8687–8692.
[31] P. Brown, C. Butts, J. Eastoe, Surfactant Ionic Liquids: Potential Structured Reaction Media?, (n.d.).
[32] M. Sabbaghan, B.M. Behbahani, Synthesis and optical properties of CuO nanostructures in imidazolium-based ionic liquids, Mater. Lett. 117 (2014) 28–30.
[33] H. Shekaari, M.T. Zafarani-Moattar, S. Faraji, Thermophysical properties of protic ionic liquids monoethanolamine, diethanolamine, and triethanolamine lactate in water, J. Chem. Eng. Data 66 (2021) 1890–1899.
[34] S. Faraji, H. Shekaari, M.T. Zafarani-Moattar, M. Mokhtarpour, Experimental studies on thermophysical properties of protic ionic liquids for thermal energy storage systems, J. Energy Storage 54 (2022) 105251.
[35] S. Faraji, H. Shekaari, M.T. Zafarani-Moattar, M. Mokhtarpour, E. Asghari, Thermal properties of phase change materials ionic liquid/fatty acids for thermal energy storage applications, J. Energy Storage 67 (2023) 107464.
[36] C. Liu, Y. Hou, Y. Li, H. Xiao, Heteroatom-doped porous carbon microspheres derived from ionic liquid-lignin solution for high performance supercapacitors, J. Colloid Interface Sci. 614 (2022) 566–573.
[37] S. Şahin, Tailor-designed deep eutectic liquids as a sustainable extraction media: an alternative to ionic liquids, J. Pharm. Biomed. Anal. 174 (2019) 324–329.
[38] B.L. Gadilohar, G.S. Shankarling, Choline based ionic liquids and their applications in organic transformation, J. Mol. Liq. 227 (2017) 234–261.
[39] X. Ren, Z. Liang, X. Zhao, Preparation of hydroxyapatite nanofibers by using ionic liquids as template and application in enhancing hydrogel performance, Front. Bioeng. Biotechnol. 11 (2023) 1247448.
[40] S. Pavlovica, A. Zicmanis, E. Gzibovska, M. Klavins, P. Mekss, (2-Hydroxyethyl) ammonium lactates—highly biodegradable and essentially non-toxic ionic liquids, Green Sustain. Chem. 1 (2011) 103–110.
[41] A.N. Mirskova, S.N. Adamovich, R.G. Mirskov, Synthesis and pharmacological activity of tris-(2-hydroxyethyl) ammonium 4-chlorophenylsulfonylacetate (sulfacetamine), Pharm. Chem. J. 46 (2012) 392–396.
[42] M. Safari-Gezaz, M. Parhizkar, E. Asghari, Investigation of the structural properties of Si4+-doped HAP coatings on Ti-6Al-4V substrate as a corrosion barrier in biomedical media, Colloids Surfaces A Physicochem. Eng. Asp. (2024) 134742.
[43] A.C. Mendhe, Spin coating: easy technique for thin films, in: Simple Chem. Methods Thin Film Depos. Synth. Appl., Springer, 2023, pp. 387–424.
[44] S.S. Nisar, H.-C. Choe, Mechanical hydroxyapatite coatings on PEO-treated Ti–6Al–4V alloy for enhancing implant's surface bioactivity, Ceram. Int. 50 (2024) 17703–17719.
[45] C.A. Poblano-Salas, J. Henao, A.L. Giraldo-Betancur, P. Forero-Sossa, D.G. Espinosa-Arbelaez, J.A. González-Sánchez, L.R. Dzib-Pérez, S.T. Estrada-Moo, I. E. Pech-Pech, HVOF-sprayed HAp/S53P4 BG composite coatings on an AZ31 alloy for potential applications in temporary implants, J. Magnesium Alloys 12 (2024) 345–360.
[46] V.C.A. Prakash, I. Venda, V. Thamizharasi, E. Sathya, A new attempt on synthesis of spherical nano hydroxyapatite powders prepared by dimethyl sulfoxide-poly vinyl alcohol assisted microemulsion method, Mater. Chem. Phys. 259 (2021) 124097.
[47] S. Mohammadi Aref, M. Safarigezaz, M. Khatamian, Synthesis of hydroxyapatite nanoparticles by the Sol-Gel method, investigation of its morphology and comparison of its structure with intact tooth, Iran, J. Phys. Res. 20 (2020) 445–453.
[48] A. Thakur, A. Kumar, S. Kaya, F. Benhiba, S. Sharma, R. Ganjoo, H. Assad, Electrochemical and computational investigations of the Thysanolaena latifolia leaves extract: an eco-benign solution for the corrosion mitigation of mild steel, Results Chem 6 (2023) 101147.
[49] A. Thakur, O. Dagdag, A. Berisha, E.E. Ebenso, A. Kumar, S. Sharma, R. Ganjoo, H. Assad, Mechanistic insights into the corrosion inhibition of mild steel by eco-benign Asphodelus tenuifolius aerial extract in acidic environment: electrochemical and computational analysis, Surf. Coating. Technol. 480 (2024) 130568.
[50] L. Hernández, J.E. González, V. Barranco, Y. Veranes-Pantoja, J.C. Galván, G.R. Gattorno, Biomimetic hydroxyapatite (HAp) coatings on pure Mg and their physiological corrosion behavior, Ceram. Int. 48 (2022) 1208–1222.
[51] J. Brzeska, A.M. Elert, M. Morawska, W. Sikorska, M. Kowalczuk, M. Rutkowska, Branched polyurethanes based on synthetic polyhydroxybutyrate with tunable structure and properties, Polymers 10 (2018) 826.
[52] V.C.A. Prakash, I. Venda, V. Thamizharasi, E. Sathya, A comparative study on microemulsion synthesis of hydroxyapatite powders by ionic and Non-Ionic surfactants, Mater. Today Proc. 51 (2022) 1701–1705.
[53] A. Aamouche, E. Goormaghtigh, FTIR-ATR biosensor based on self-assembled phospholipids surface: haemophilia factor VIII diagnosis, Spectroscopy 22 (2008) 223–234.
[54] J. Coates, Interpretation of Infrared Spectra, a Practical Approach, 2000.
[55] C.M. Botelho, M.A. Lopes, I.R. Gibson, S.M. Best, J.D. Santos, Structural analysis of Si-substituted hydroxyapatite: zeta potential and X-ray photoelectron spectroscopy, J. Mater. Sci. Mater. Med. 13 (2002) 1123–1127.
[56] S. Jarudilokkul, W. Tanthapanichakoon, V. Boonamnuayvittaya, Synthesis of hydroxyapatite nanoparticles using an emulsion liquid membrane system, Colloids Surfaces A Physicochem. Eng. Asp. 296 (2007) 149–153.
[57] A. Kaflak, W. Kolodziejski, Complementary information on water and hydroxyl groups in nanocrystalline carbonated hydroxyapatites from TGA, NMR and IR measurements, J. Mol. Struct. 990 (2011) 263–270.
[58] M. Safari-Gezaz, M. Mirzaei-Saatlo, E. Asghari, M. Parhizkar, The incorporation of cobalt ions into hydroxyapatite nanostructure for a novel range of electrochemical energy storage applications, J. Phys. Chem. Solid. (2024) 112118.
[59] V.C.A. Prakash, I. Venda, V. Thamizharasi, Synthesis and characterization of surfactant assisted hydroxyapatite powder using microemulsion method, Mater. Today Proc. 51 (2022) 1788–1792.

[60] S. Akter, M. Yousuf, A. Mollah, A. Samina, N.-H.P. from Eggshell-Derived, CalciumPrecursor using reverse microemulsions as nanoreactor biomater, Artif. Organs 4 (2017) 5497–5506.
[61] K. Behera, S. Pandey, Ionic liquid induced changes in the properties of aqueous zwitterionic surfactant solution, Langmuir 24 (2008) 6462–6469.
[62] Z. He, P. Alexandridis, Nanoparticles in ionic liquids: interactions and organization, Phys. Chem. Chem. Phys. 17 (2015) 18238–18261.
[63] G. Çelebi Efe, E. Yenilmez, Study on surface properties of UHMWPE/Hap composite coating on Ti6Al4V, Surf. Eng. 38 (2022) 417–429.
[64] J. Singh, S.S. Chatha, H. Singh, Synthesis and characterization of plasma sprayed functional gradient bioceramic coating for medical implant applications, Ceram. Int. 47 (2021) 9143–9155.
[65] R. Khoramian, M. Issakhov, P. Pourafshary, M. Gabdullin, A. Sharipova, Surface modification of nanoparticles for enhanced applicability of nanofluids in harsh reservoir conditions: a comprehensive review for improved oil recovery, Adv. Colloid Interface Sci. (2024) 103296.
[66] R. Rohrbaugh, M. McDonald, J. Carter, E. Gosselink, C. Ghosh, G. Jordan, H. O'Connor, H. Liddle, M. Evers, Coating Compositions for Modifying Hard Surfaces, 2002.
[67] H. Daugaard, B. Elmengaard, J.E. Bechtold, T. Jensen, K. Soballe, The effect on bone growth enhancement of implant coatings with hydroxyapatite and collagen deposited electrochemically and by plasma spray, J. Biomed. Mater. Res. Part A An Off. J. Soc. Biomater. Japanese Soc. Biomater. Aust. Soc. Biomater. Korean Soc. Biomater. 92 (2010) 913–921.
[68] R.B. Heimann, Functional plasma-sprayed hydroxylapatite coatings for medical application: clinical performance requirements and key property enhancement, J. Vac. Sci. Technol. A 39 (2021).
[69] S. Awasthi, S.K. Pandey, E. Arunan, C. Srivastava, A review on hydroxyapatite coatings for the biomedical applications: experimental and theoretical perspectives, J. Mater. Chem. B 9 (2021) 228–249.
[70] P. Mandracci, F. Mussano, P. Rivolo, S. Carossa, Surface treatments and functional coatings for biocompatibility improvement and bacterial adhesion reduction in dental implantology, Coatings 6 (2016) 7.
[71] B. Priyadarshini, U. Vijayalakshmi, In Vitro bioactivity, biocompatibility and corrosion resistance of multi-ionic (Ce/Si) co-doped hydroxyapatite porous coating on Ti-6Al-4 V for bone regeneration applications, Mater. Sci. Eng. C 119 (2021) 111620.
[72] D.D. Deligianni, N.D. Katsala, P.G. Koutsoukos, Y.F. Missirlis, Effect of surface roughness of hydroxyapatite on human bone marrow cell adhesion, proliferation, differentiation and detachment strength, Biomaterials 22 (2000) 87–96.
[73] H. Li, K.A. Khor, P. Cheang, Titanium dioxide reinforced hydroxyapatite coatings deposited by high velocity oxy-fuel (HVOF) spray, Biomaterials 23 (2002) 85–91.
[74] M.A. Valadez-Martínez, L.G. Hernández-Maya, I.A. Avelino-Jiménez, J. Menchaca-Arredondo, V. Garibay-Febles, I. Zapata-Peñasco, Influence of roughness on the early corrosion of API steels by atomic force microscopy (AFM): a real-time assessment, Mater. Today Commun. 36 (2023) 106519.
[75] S.A.X. Stango, U. Vijayalakshmi, Synthesis and characterization of hydroxyapatite/carboxylic acid functionalized MWCNTS composites and its triple layer coatings for biomedical applications, Ceram. Int. 45 (2019) 69–81.
[76] H. Jamali, S. Moradi-Alavian, E. Asghari, M.D. Esrafili, E. Payami, R. Teimuri-Mofrad, Prolonged corrosion protection via application of 4-ferrocenylbutyl saturated carboxylate ester derivatives with superior inhibition performance for mild steel, Sci. Rep. 14 (2024) 13847.
[77] D. Sharma, A. Thakur, M.K. Sharma, A. Bhardwaj, A. Sihmar, H. Dahiya, A.K. Sharma, A. Kumar, A. Berisha, H. Om, Experimental and computational studies on the corrosion inhibition potential of a novel synthesized thiophene and pyridine-based 1, 3, 4-oxadiazole hybrid against mild steel corrosion in 1 N HCl, Environ. Sci. Pollut. Res. (2024) 1–27.
[78] V.C. Anadebe, F.E. Abeng, A. Thakur, K.P. Katin, E. Berdimurodov, T.C. Egbosiuba, E.E. Ebenso, Surface interaction and inhibition mechanism prediction of Aciclovir molecule on Fe (110) using computational model based on DFT, RDF and MD simulation, Comput. Theor. Chem. (2024) 114702.
[79] M. Mirzaei-Saatlo, H. Jamali, S. Moradi-Alavian, E. Asghari, R. Teimuri-Mofrad, M.D. Esrafili, 4-Ferrocenylbutyl-based corrosion inhibitors for mild steel in acidic solution, Mater. Chem. Phys. 293 (2023) 126895.
[80] B. El Ibrahimi, Atomic-scale investigation onto the inhibition process of three 1, 5-benzodiazepin-2-one derivatives against iron corrosion in acidic environment, Colloid Interface Sci. Commun. 37 (2020) 100279.
[81] D. Seifzadeh, E. Golmoghani-Ebrahimi, Formation of novel and crack free nanocomposites based on sol gel process for corrosion protection of copper, Surf. Coating. Technol. 210 (2012) 103–112.
[82] A. Baddouh, G.G. Bessegato, M.M. Rguiti, B. El Ibrahimi, L. Bazzi, M. Hilali, M.V.B. Zanoni, Electrochemical decolorization of Rhodamine B dye: influence of anode material, chloride concentration and current density, J. Environ. Chem. Eng. 6 (2018) 2041–2047.
[83] S. Kaya, H. Lgaz, A. Thakkur, A. Kumar, D. Özbakır Işın, N. Karakuş, S. Ben Ahmed, Molecular insights into the corrosion inhibition mechanism of omeprazole and tinidazole: a theoretical investigation, Mol. Simulat. 49 (2023) 1632–1646.
[84] D. Sharma, A. Thakur, M.K. Sharma, A. Kumar, K. Jakhar, S. Kumar, A. Sihmar, H. Dahiya, A. Kumar, A.K. Sharma, A convenient synthesis, electrochemical profiling, and morphological studies of a pyridine-based 1, 3, 4-oxadiazole hybrid: a promising study for corrosion mitigation of mild steel in strongly acidic environment, Inorg. Chem. Commun. 158 (2023) 111554.
[85] S. Eloul, C. Batchelor-McAuley, R.G. Compton, Thin film-modified electrodes: a model for the charge transfer resistance in electrochemical impedance spectroscopy, J. Solid State Electrochem. 18 (2014) 3239–3243.
[86] G. Pedrizzetti, L. Paglia, V. Genova, S. Cinotti, M. Bellacci, F. Marra, G. Pulci, Microstructural, mechanical and corrosion characterization of electroless Ni-P composite coatings modified with ZrO2 reinforcing nanoparticles, Surf. Coating. Technol. 473 (2023) 129981.
[87] S. Xu, Y. Zheng, F. Zhan, P. La, Microstructure evolution and molten salt corrosion resistance dependent on pre-oxidation treatment of NiAl coatings, Sci. Adv. Mater. 16 (2024) 731–740.
[88] P. Perumal, K. Ramanathan, L. Ganesan, B. Subramanian, V. Ganesh, B. Stalin, Investigation of TiN coating uniformity and its corrosion behaviour using image process, Mater. Res. Express 6 (2019) 46411.
[89] M. Puig, L. Cabedo, J.J. Gracenea, A. Jiménez-Morales, J. Gámez-Pérez, J.J. Suay, Adhesion enhancement of powder coatings on galvanised steel by addition of organo-modified silica particles, Prog. Org. Coating 77 (2014) 1309–1315.
[90] M. Afshari, H.E. Mohammadloo, A.A. Sarabi, S. Roshan, Modification of hydroxyapatite-based coating in the presence of polyvinylalcohol (PVA) for implant application: corrosion, structure and surface study, Corrosion Sci. 192 (2021) 109859.
[91] A. Shanaghi, B. Mehrjou, Z. Ahmadian, A.R. Souri, P.K. Chu, Enhanced corrosion resistance, antibacterial properties, and biocompatibility by hierarchical hydroxyapatite/ciprofloxacin-calcium phosphate coating on nitrided NiTi alloy, Mater. Sci. Eng. C 118 (2021) 111524.
[92] A. Zomorodian, C. Santos, M.J. Carmezim, T.M. e Silva, J.C.S. Fernandes, M. de F. Montemor, "In-vitro" corrosion behaviour of the magnesium alloy with Al and Zn (AZ31) protected with a biodegradable polycaprolactone coating loaded with hydroxyapatite and cephalexin, Electrochim. Acta 179 (2015) 431–440.
[93] E.-J. Kim, Y.-H. Jeong, H.-C. Choe, W.A. Brantley, Electrochemical behavior of hydroxyapatite/TiN multi-layer coatings on Ti alloys, Thin Solid Films 572 (2014) 113–118.
[94] X. Zhang, Y. Wu, Y. Lv, Y. Yu, Z. Dong, Formation mechanism, corrosion behaviour and biological property of hydroxyapatite/TiO2 coatings fabricated by plasma electrolytic oxidation, Surf. Coating. Technol. 386 (2020) 125483.
[95] A.S. Gnedenkov, S.L. Sinebryukhov, V.S. Filonina, S. V Gnedenkov, Hydroxyapatite-containing PEO-coating design for biodegradable Mg-0.8 Ca alloy: formation and corrosion behaviour, J. Magnesium Alloys 11 (2022) 4468–4484.
[96] S. Singh, K.K. Pandey, A.K. Keshri, Effect of plasma power on corrosion behaviour of plasma sprayed hydroxyapatite coatings, Met. Mater. Int. 27 (2021) 4455–4462.